A numerical study on the effect of loading and randomness on fracture patterns in a tight formation

Abedi, R.,
Department of Mechanical, Aerospace & Biomedical Engineering, The University of Tennessee Space Institute, TN, USA

Omidi, O.
Department of Civil, Environmental & Architectural Engineering, The University of Kansas, KS, USA

Clarke, P.L.
Department of Mechanical, Aerospace & Biomedical Engineering, The University of Tennessee Space Institute, TN, USA

ABSTRACT: Hydraulic fracturing has been the most common approach to stimulate tight formations. The geometry of the wellbore and the time history of the hydraulic loading play important roles in induced fracture patterns. For example, generating multiple perforations in a wellbore is nowadays attracting more attention in oil industry to enhance gas recovery. The increased number of fractures can potentially enhance the yield of a reservoir by increasing the regions affected by hydraulic fractures. We use an *h*-adaptive spacetime discontinuous Galerkin method and an interfacial damage model to study the conditions for which the induced hydraulic fractures become effective and propagate in rock. Our results show that as the loading rate decreases, only a few of these fractures will propagate. As the loading rate increases, more perforations become active, until ultimately all result in crack propagation. Moreover, higher loading rates affect larger zones for each of the initial perforations by dynamic fracture features such as microcracking and crack bifurcation. Our study mainly focuses on stimulation techniques that induce fully dynamic loading on rocks; for example, high explosives detonate and sends a shock wave in rock. Given the limitations of hydraulic fracturing technique, we study the effectiveness of a hybrid approach where initial perforations similar to those for hydraulic fracturing are used as seeds of crack propagation under dynamic loading. Finally for very high rates of loading, we demonstrate that a stochastic approach for crack nucleation predicts more realistic fracture patterns than conventional approaches that assume a macroscopically uniform fracture strength for rock.

1 INTRODUCTION

Generating fractures in deep and tight formations has received a high priority in oil industry to enhance the productivity of low permeability reservoirs which are already in operation. The induced fractures interacting with natural fractures form an interface with rock matrix and the borehole to facilitate the oil extraction. In fact, fracture volume induced by a stimulation technique is negligible in comparison with the total reservoir volume; however, they provide an interface with matrix which is larger than the borehole. As a result, very small permeability values are sufficient for production in a fractured tight formation. Therefore, the formation of fracture networks with a widespread pattern is a critical key in increasing pro-

duction of tight oil reservoirs. Some geological factors highly affect the formation of fracture networks: rock mineral composition, rock mechanical properties, natural fractures and stress field. The orientation of the natural fractures and the stress anisotropy in fractured formations highly affect the propagation of the hydraulic fracture and the formation of fracture networks [1, 2].

The results observed by Vishkai *et al.* [3] illustrate the importance of rock properties, stress magnitude, and stress orientation on fracture pattern in unconventional naturally fractured reservoirs. Bahrami *et al.* highlighted the significance of well completion system, horizontal well orientation, and direction of in-situ horizontal stresses in controlling well productivity [4]. That is, relative magnitude of in-

situ stresses and their direction can control production performance of non-fractured and hydraulically fractured horizontal wells in unconventional gas reservoirs. Besides, fracture initiation and propagation in quasi-brittle materials under strain-controlled loading is highly sensitive to strain rate. Using a two dimensional Discrete Element Method (DEM), Tomac *et al.* investigated a hypothesis that fluid pressurization rate or the fluid flow rate influences the character, shape and velocity of fracture propagation in rock [5]. Their results indicate that very high fluid flow rates cause fracture arrest and multiple fracture branching from the borehole. Moreover, they show that the relative compressibility of fracturing fluid and rock plays a significant role in fracture propagation velocity. In fact, the rapid build-up of the pressure in the wellbore, in absence of the inflow of the fluid into initiated fracture, causes creation of multiple simultaneous fracture branches at the wellbore wall [5]. For tight formations and low permeable rocks, under high loading rates the predicted tensile crack lengths are relatively small due to the possibility that alternative deformation mechanisms such as shear cracking or propagation of the pre-existing flaw are activated at high rates [6].

According to the rate at which energy is applied, well stimulation technologies can generally be categorized into three approaches. At one extreme conventional, hydraulic fracturing, having a relatively low rate of loading, results in a single bi-winged fracture extending outward from a well, oriented perpendicular to the least principal rock stress while the potential penetration for the fracture can be large, hundreds of feet. However, having multiple perforations is not beneficial and in fact those would not be activated in this technique. On the other extreme, explosive fracturing, having a very rapid loading rate, results in a highly fractured zone radially around the wellbore, but usually not exceeding 10 feet. However, high induced compressive stresses in the vicinity of the wellbore can cause compaction decreasing the permeability of the near-wellbore region as a damaged zone. Pulse fracturing is between these two extremes of the loading rates. Avoiding the damage associated with the explosive fracturing approach, this technique creates a radial fracture pattern, which is desirable. This technique results in multiple fractures extending radially from the wellbore with penetration on the order of 10-20 feet. For example, propellant fracturing involving the pressure build-up due to propellant burning accompanied by a gas combustion is a kind of pulse fracturing methods. Pulse fracturing is also included in the early stage of conventional hydraulic

fracturing when a high loading rate is applied as an instantaneous fracture creation and propagation after wellbore breakdown. The combination of pulse and hydraulic fracturing holds promise for tight formations as a hybrid method [7].

Considering two approaches of deterministic and stochastic crack nucleation models, we perform a sensitivity analysis to examine the effect of loading rate on resulting fracture patterns. A probabilistic nucleation model based on the Weibull model is proposed to model heterogeneity of rock strength around a wellbore. In §2, we briefly discuss the formulation of an interfacial damage model and an *h*-adaptive Spacetime Discontinuous Galerkin (SDG) method for fracture simulation of rocks. Of particular importance to hydraulic fracturing is the ability of SDG method to align inter-element boundaries with user-specified interfaces in spacetime. Also, the interfacial damage model captures modes I and II of intact material breakage as well as shearing along newly created and pre-existing fractures [8, 9]. Finally, in §3, we qualitatively study the crack patterns obtained by changing the rate of loading. We demonstrate that as the loading rate increases, more dynamic brittle fracture features such as microcracking and crack branching occur and that high-rate loading provides a mechanism to activate all initial perforations from the wellbore wall. Our results also demonstrate that incorporating material inhomogeneities is particularly important under very high strain-rate loading conditions.

2 FORMULATION

2.1 A traction-displacement controlled damage model

In this work we use a sharp interfacial model to represent mechanical degradation in rock. The damage model presented in [10, 11] has several advantages over conventional cohesive models, in that it incorporates rate effects and unlike intrinsic cohesive models does not artificially increase the compliance of the bulk [12]. Furthermore, it seamlessly incorporates all dynamically consistent contact modes. Albeit all these advantages, the aforementioned damage model suffers from the possibility of having incomplete damage when an interface is and must be physically fully debonded.

The following sections describe three main components of the damage model. In §2.1.1 dynamically consistent solutions for different contact / separation modes are discussed. An averaging scheme that combines these contact solutions to form macro-

scopic target solutions is described in §2.1.2. Finally, the derivation of the weights by which these solutions are combined is discussed in §2.1.3. Specifically, in the last section we describe how a new damage evolution equation remedies the incomplete damage problem with the models in [10, 11].

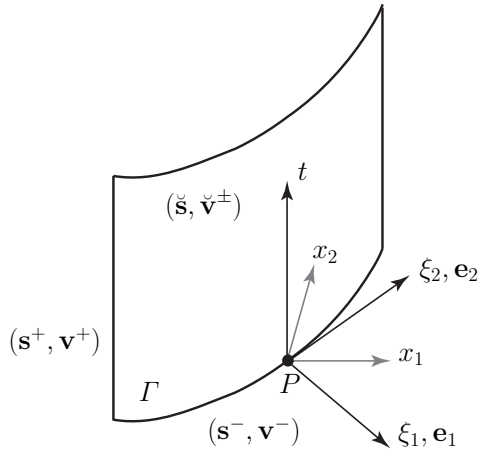### 2.1.1 Riemann solutions for different contact modes

Figure 1: Local coordinate frame at arbitrary spacetime location P on a spacetime fracture surface Γ for a problem in two spatial dimensions.

The solutions for individual contact modes are obtained by solving local Riemann problems at a contact interface. A local coordinate frame at an arbitrary spacetime location P on contact interface Γ is illustrated in fig. 1. The local coordinates are (ξ_1, ξ_2, t), and the frame is oriented such that the ξ_1-direction aligns with the spatial normal vector on Γ.

The quantities from the opposite sides of Γ, which are decorated with superscripts $+$ and $-$, define the initial data for the Riemann problem. The normal vector is oriented from side $+$ to $-$ and is used to express the components of traces of velocities $\mathbf{v}^\pm$ and tractions, $\mathbf{s}^\pm$. Tractions are computed from $\mathbf{s}^\pm = \boldsymbol{\sigma}^\pm \mathbf{n}$ where $\boldsymbol{\sigma}^\pm$ are traces of stress tensor. The Riemann values at a given point P on the interface include components of the traction vector acting on the interface and traces of the velocity components from each side of the interface. We denote these by $(\check{\mathbf{s}}, \check{\mathbf{v}}^\pm)$, as shown in the figure. Depending on the form of kinematic compatibility condition for a given contact mode, all, some, or none of the components of target velocities $\check{\mathbf{v}}^\pm$ may suffer jump across the interface. On the other hand, target traction $\check{\mathbf{s}}$ is uniquely defined from the balance of linear momentum.

For linear elastodynamic problem, characteristic values are preserved along characteristic directions. For an isotropic material, characteristic directions move in spacetime with dilatational and shear wave speeds, $c_d^\pm$ and $c_s^\pm$,

$$c_\mathrm{d} = \sqrt{\frac{\lambda + 2\mu}{\rho}}, \qquad c_\mathrm{s} = \sqrt{\frac{\mu}{\rho}}. \tag{1}$$

where ρ is the mass density and λ, μ are the Lamé parameters. Subsequently, impedance values, given by,

$$Z^{i\pm} := \begin{cases} (c_d\rho)^\pm & i = 1 \\ (c_s\rho)^\pm & i = 2, 3 \end{cases} \tag{2}$$

are used to define characteristic values. The preservation of characteristic values from each side and enforcement of appropriate kinematic condition are used to derived Riemann solutions for various contact modes [13]. Specifically, boded and contact–stick solutions, decorated with ST and B respectively, are,

$$\check{s}_\mathrm{B}^i = \check{s}_\mathrm{ST}^i = \check{s}^i = \frac{s^{i+}Z^{i-} + s^{i-}Z^{i+}}{Z^{i-} + Z^{i+}} + \frac{Z^{i-}Z^{i+}}{Z^{i-} + Z^{i+}}(v_i^+ - v_i^-) \tag{3a}$$

$$\check{v}_i^\mathrm{B} = \check{v}_i^\mathrm{ST} = \check{v}_i = \frac{s^{i-} - s^{i+}}{Z^{i-} + Z^{i+}} + \frac{v_i^+ Z^{i+} + v_i^- Z^{i-}}{Z^{i-} + Z^{i+}} \tag{3b}$$

For the separation mode, no kinematic compatibility condition is enforced across the interface, hence $\check{\mathbf{v}}^+$ and $\check{\mathbf{v}}^-$ are independent. Similar to TSRs, where target traction is obtained by displacement jump across the interface, a constitutive model is used to obtain separation traction $\mathbf{S}$. Accordingly, Riemann solutions for separation mode, decorated by S, are obtained as,

$$\check{s}_\mathrm{S}^i = \check{s}^i = S^i \tag{4a}$$

$$\check{v}_i^{\mathrm{S}\pm} = \check{v}_i^\pm = v_i^\pm \pm \frac{S^i - s^{i\pm}}{Z^{i\pm}} \tag{4b}$$

The prescribed traction vector $\mathbf{S}$ can take different forms. For example, similar to TSRs, $\mathbf{S}$ can be expressed as a function of the displacement jump across the interface. For hydraulic fracture applications S^1 is set equal to the applied hydraulic pressure. Riemann solutions for contact–slip modes are the last case to be considered. However, due to more complexity of those solutions and not a direct relation to the material herein, we refer the readers to [13] for further detail on contact–slip solutions.

3

2.1.2 Macroscopic target values

The macroscopic target traction vector $\mathbf{s}^*$ and velocity vectors $\mathbf{v}^{*\pm}$ are obtained by using an interfacial damage parameter D which interpolates between *bonded* and *debonded* target solutions,

$$\mathbf{s}^* := (1 - D)\breve{\mathbf{s}}_B + D\breve{\mathbf{s}}_D \tag{5a}$$

$$\mathbf{v}^{*\pm} := (1 - D)\breve{\mathbf{v}}_B + D\breve{\mathbf{v}}_D^{\pm} \tag{5b}$$

where subscripts B and D indicate Riemann values for bonded (*cf.* (3)) and debonded conditions. For the debonded part, either contact–stick (3), contact–slip, or separation (4) solutions hold. Clearly, for problems that contact modes do not occur, $\breve{\mathbf{s}}_D = \mathbf{S}$ and $\mathbf{v}^{*\pm} = \breve{\mathbf{v}}^{\mathbf{S}\pm}$. The details on the form of debonded solutions, when contact modes can exist, can be found in [13].

2.1.3 Damage evolution law

We adopt the following damage evolution law,

$$\dot{D} = \begin{cases} \frac{1}{\tilde{\tau}}[1 - H(\langle D_t - D\rangle_+)] & D < 1 \\ 0 & D = 1 \end{cases}, \tag{6}$$

where $\tilde{\tau}$ is a *relaxation time*, and D_t is the *target damage value*. The function H takes the value of unity at zero and monotonically decreases to 0 at infinity. Following [14], the particular form of H used in this work is given as $H(x) = \exp(-ax)$. It is clear from (6) that when loading monotonically increases at a time scale much slower than $\tilde{\tau}$, $\langle D_t - D\rangle_+ \to 0$ and $D \to D_t$. That is, the target damage value D_t is in fact quasi-static damage value under monotonically increasing loading condition. Finally, the positive part operator in $\langle D_t - D\rangle_+$ ensures that D can only change (increase) when target damage value is larger than the present damage value, *i.e.,* under loading conditions.

We stipulate D_t to be a function of acting tractions and separation vector. More specifically, we assume D_t to be expressed as,

$$D_t = g(\breve{s}, \breve{\delta}) \tag{7}$$

where $\breve{s}$ is a scalar stress quantity, labeled as *effective stress*, and $\breve{\delta}$ is the *effective displacement jump* as discussed below. Experimental studies such as [15, 16] demonstrate that damage evolution on an interface is mainly stress-driven. In the proposed damage model, the interface is divided in the two parts of bonded and debonded which conceptually take $(1 - D)$ and D area fractions of the interface at a point. Since the bonded part resists crack opening, it is the traction acting on the bonded part, *i.e.,* $\breve{\mathbf{s}}_B$ from (3a), that

drives damage evolution. While the dependence of $\breve{s}$ on $\breve{\mathbf{s}}_B$ can be calibrated experimentally, we adopt the definition of effective stress from [17],

$$\breve{s} := \sqrt{\langle \breve{s}_B^1 \rangle_+^2 + \beta_s^2 \left[\left(\breve{s}_B^2 \right)^2 + \left(\breve{s}_B^3 \right)^2 \right]} \tag{8}$$

where β_s is the *shear stress factor*; the larger β_s, the more sensitive is fracture response to shear stress at the interface. The positive-part operator $\langle . \rangle_+$ ensures that only tensile mode of normal traction drives damage evolution.

The effective displacement is a scalar function of displacement jump $\boldsymbol{\delta} := \mathbf{u}^- - \mathbf{u}^+$ where $\mathbf{u}^-$ and $\mathbf{u}^+$ are the interior traces of the displacement vector from the two sides of the interface. Again motivated by the definition of effective quantities in [17] we adopt the following definition for $\breve{\delta}$,

$$\breve{\delta} := \sqrt{\langle \delta_1 \rangle_+^2 + \beta_\delta^2 \left(\delta_2^2 + \delta_3^2 \right)} \tag{9}$$

where similar to previous case, *displacement mode mixity* β_δ signifies the importance of tangential displacement jump relative to normal separation and the positive part operation for $\langle \delta_1 \rangle_+$ ensures that damage does not accumulate by interface penetration.

To define the dependency of D_t on $\breve{s}$ and $\breve{\delta}$ in (7) we define *traction target damage* D_t^s and *displacement jump target damage* D_t^δ as,

$$D_t^s = \begin{cases} 0 & \breve{s} < \underline{s}, \\ \frac{\breve{s} - \underline{s}}{\bar{s} - \underline{s}} & \underline{s} \le \breve{s} < \bar{s} , \\ 1 & \bar{s} \le \breve{s} \end{cases} \tag{10a}$$

$$D_t^\delta = \begin{cases} 0 & \breve{\delta} < \underline{\delta}, \\ \frac{\breve{\delta} - \underline{\delta}}{\bar{\delta} - \underline{\delta}} & \underline{\delta} \le \breve{\delta} < \bar{\delta} , \\ 1 & \bar{\delta} \le \breve{\delta} \end{cases} \tag{10b}$$

where $\underline{s}$ and $\bar{s}$ denote, respectively, effective traction thresholds for the onset of additional traction damage evolution and for attainment of the maximum damage rate. The displacement scales $\underline{\delta}$ and $\bar{\delta}$ have a similar interpretation and meaning to those from (10a) but for displacement jump damage parameter D_t^δ. Finally, D_t in (7) can in turn be expressed as a function of D_t^s and D_t^δ. For example, we use the following function,

$$D_t = \min\left(\sqrt{\left(D_t^s\right)^2 + \left(D_t^\delta\right)^2}, 1 \right) \tag{11}$$

A detailed analysis, which is not provided herein for brevity, shows that the definition of D_t in (11) remedies the incomplete damage problem of models in [10, 11].

2.2 Probabilistic model for crack nucleation and propagation

While the probabilistic crack nucleation model and spacetime adaptive crack tracking scheme in this section are described in [8], a short description is provided for completeness and better interpretation of results in §3 (particularly §3.2).

The fracture response of many quasi-brittle materials, including rocks, is highly sensitive to their microstructural defects Fracture models that assume uniform material properties can predict very unrealistic fracture responses particularly for quasi-brittle materials given their high sensitivity to microstructural defects. In addition, for cases where a rather uniform stress field is experienced the homogeneity of fracture properties can result in rather instantaneous fracture initiation at many points in the domain as they all experience almost the same stress field and have identical fracture strengths.
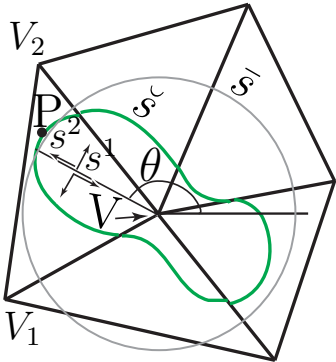
Figure 2: The angular distribution of effective stress $\check{s}$ and fracture strength $\bar{s}$ around vertex V at the top of a patch.

We base our probabilistic crack nucleation criteria on the Weibull model [18, 19], since it can reasonably well model probabilistic fracture strength and size effect of quasi-brittle materials such as rock. The *cumulative distribution function* (CDF) for fracture strength $\bar{s}$, *cf.* (10a), is given by,

$$P(\check{s}) = 1 - e^{-\frac{A}{A_0} \left(\frac{\check{s} - s_{\min}}{s_0} \right)^m} \tag{12}$$

in which A_0 is a reference area, such as the area of an experimental rock specimen used to calibrate the Weibull model, s_0 is a strength scale, m is the Weibull modulus, and $s_{\min}$ is a lower bound for the fracture strength. Lower values for s_0 imply lower fracture strengths, $\bar{s}$.

Figure 2 illustrates how the Weibull model is used to nucleate new cracks in discrete setting. An *h*-adaptive spacetime discontinuous Galerkin method

[20–22] advances the solution by erecting a patch, small collection of elements, around a vertex in time. The patch of elements around vertex V in fig. 2, has a spatial area of A. This area represents the sample area used in the Weibull model in (12). Accordingly, a random strength $\bar{s}$ is sampled for the vertex V based on the calibrated Weibull model. The gray circle in fig. 2 depicts angular-independent $\bar{s}$, where distance to vertex V indicates the value of $\bar{s}$ for a given potential crack propagation angle θ. The fracture strength is compared with effective stress $\check{s}$ computed from (8) for any potential crack propagation angle θ. The radial distribution of $\check{s}$ is shown by the green line in the figure, where again distance to vertex V indicates the value. If for a point such as P effective stress $\check{s}(\theta)$ is a local maximum and exceeds $\bar{s}$, vertex V becomes an *Active Crack Tip* (ACT) and a crack propagation from V, aligned with the direction corresponding to maximum effective stress, is requested. Finally, the SDG method's powerful adaptive operations in spacetime enable aligning element boundaries with any requested crack direction. For example, in fig. 2 either the element V-V1-V2 is refined along V1-V2 to align a new element edge with VP direction, or the edge V-V2 is gradually aligned with VP in spacetime; for more information please refer to [10, 11].

3 NUMERICAL RESULTS

Wellbores are commonly cased and then perforated before starting hydraulic fracturing for stability concerns and for isolating the well from undesirable regions. These perforations generated during the process of a well completion play the role of a transmission channel between the wellbore and the reservoir. In fact, a perforation may serve as an initial fracture to help with crack nucleation. As sketched in fig. 3, an application with phasing angles of 90° is considered. The domain is a 2m × 2m square. All problems considered use the confinement pressures $\sigma_h = \sigma_H = 2.425$ MPa, unless otherwise mentioned.
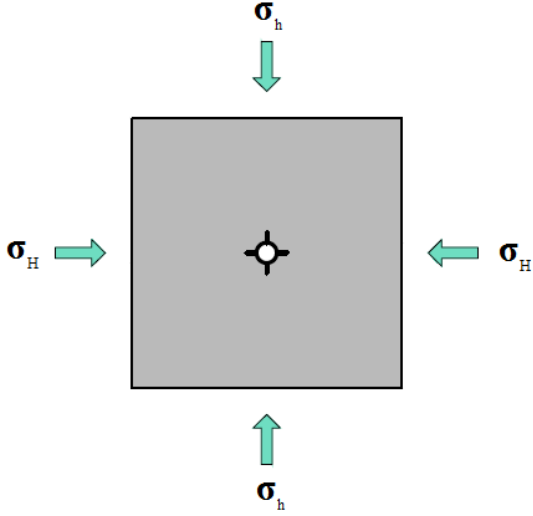
Figure 3: Problem sketch for the dynamic fracturing in a well with four perforations

In this section we study the effect of loading rate and the choice of nucleation model. Dynamic stimulation methods are often associated with explosive or propellant methods. While these approaches are typically performed without any initial perforations, [7] shows that the existence of some initial perforations greatly improves the connectivity of induced fracture network and recovery of the reservoir. The durations at which the loads are applied with these hybrid approaches approximately range from 1 to 100 ms. Also, while a single hydraulic fracturing injection often takes a duration in the order of minutes, the studies that consider the early pump-in stage in the area close to the well [23], or consider more dynamic and/or cyclic application of loading [24, 25] deal with load ramp times in the range 0.1 to 10 s. Finally, in §3.2 we demonstrate that as the loading rate increases, it becomes more imperative to use a fracture model that does not treat rock as a medium with uniform strength at macroscale. Accordingly, to better emphasize this point and cover the range of relevant ramp times discussed above, we have considered loadings with ramp times ranging from 10 μs to 1 s in this section.

We use the same material and interface properties for all the problems considered herein: Young's modulus $E = 20$ GPa, mass density $\rho = 2500$ kg/m^3, Poisson's ratio $\nu = 0.20$, and relaxation time $\tilde{\tau} = 30$ ms. For the Weibull model we use the parameters $m = 4$, $\eta = 3.8$ MPa, $s_{\min} = 500$kPa, and $A_0 = 1$m^2. Setting $A = 4$m^2 (the area of the domain), in (12) the Weibull model yields the mean value $\mathbb{E}(\bar{s}) = 2.9$ MPa and standard deviation $\text{SDV}(\bar{s}) = 683$ kPa for fracture strength in the analysis domain. For the deterministic approach in §3.2 a constant value of fracture

strength is used and set to the reference value from the Weibull model.

3.1 Effect of rate of loading on fracture patterns

Figures 4, 5, and 6 show time sequences of solutions for fast ($t_r = 10$ μs), intermediate ($t_r = 1$ ms), and slow ($t_r = 100$ ms) loading rates, respectively. The strain energy density is mapped to color with blue to red colors corresponding to zero to high values. The kinetic energy density is mapped to height field. For fast loading rate, $t_r = 10$ μs, we clearly observe sharp wave fronts scattering inside the domain, *cf.* figs. 4(a-c). The existence of regions of high kinetic and strain energy densities corresponds to a highly transient crack propagation regime for $t_r = 10$ μs. Also, due to the high input power to the system not only cracks propagate from all four perforations, but also they bifurcate almost immediately after the application of the load.

In comparison, figs. 5(a-c) show a less dynamic propagation mode in the early stages for the intermediate loading rate case. It is not until times slightly before $t = 800$ μs in fig. 5d that all the main cracks are bifurcated. At the later stages in figs. 5(e-f) crack propagation becomes more transients, as the cracks have accelerated sufficiently to bifurcate and induce side microcracks. Finally, we present the results for $t_r = 100$ ms in fig. 6. Some major differences between this case and the more dynamic loadings is that cracks propagate only from two perforations and that much larger crack openings are observed at later stages of crack propagation as shown in fig. 6f.

In fig. 7 we show the space meshes at late stages of crack propagation for all different loading rates. We observe that the solutions for the shortest ramp times in figs. 7a and 7b are very similar, with both exhibiting almost immediate crack bifurcation at the base of all four perforations. As the ramp time increases further in figs. 7c and 7d, cracks take a smoother path and there are fewer bifurcation events. Finally, past the ramp time $t_r = 100$ ms and in figs. 7e and 7f we observe that two of the perforations do not result in any crack propagation. This is expected from numerous quasi-static hydraulic fracture simulations in the literature that demonstrate the same phenomena.
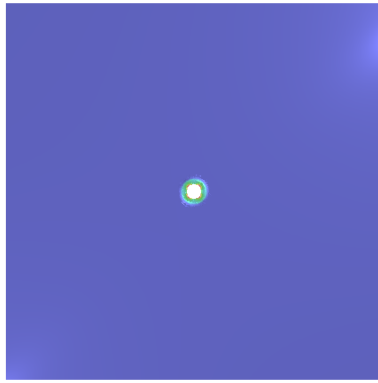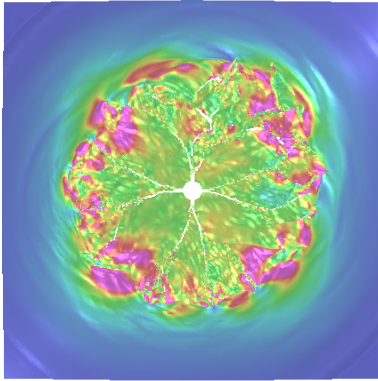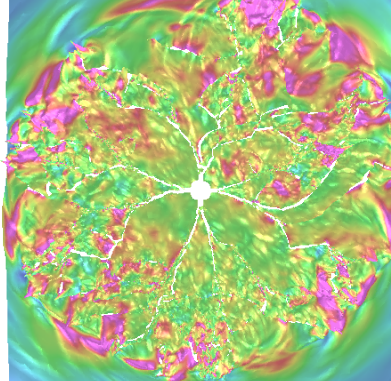
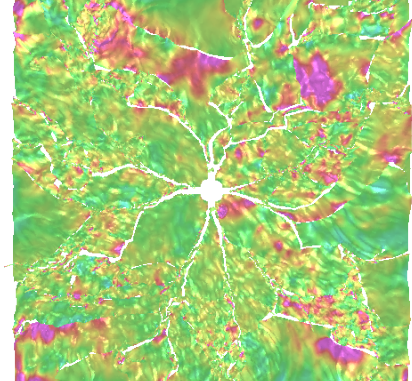(a) Time $t = 25$ μs.
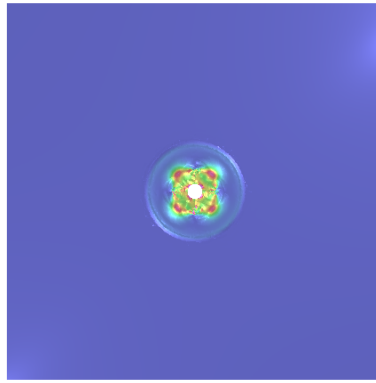
(b) Time $t = 150$ μs.
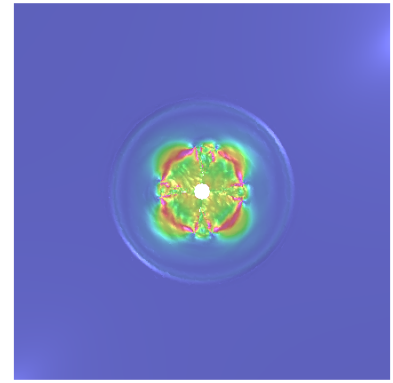
(c) Time $t = 300$ μs.
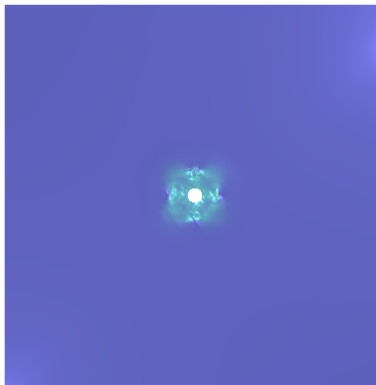
(d) Time $t = 800$ μs.

(e) Time $t = 1.2$ ms.
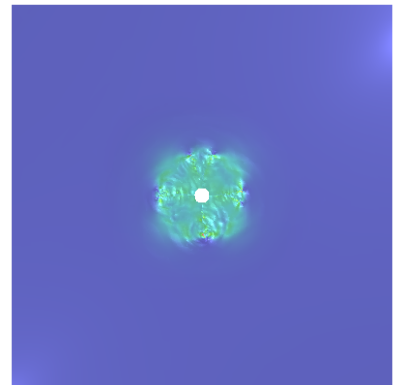
(f) Time $t = 1.7$ ms.

Figure 4: Solution visualization of well stimulation for $t_r = 10$ μs and random nucleation model.

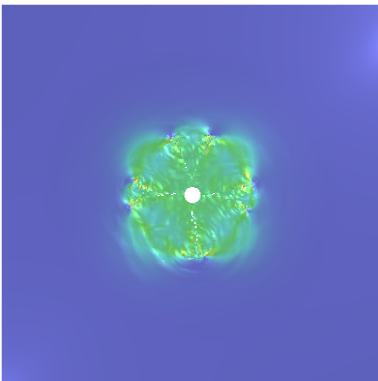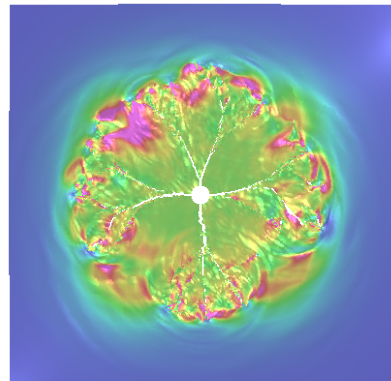(a) Time $t = 400$ μs.
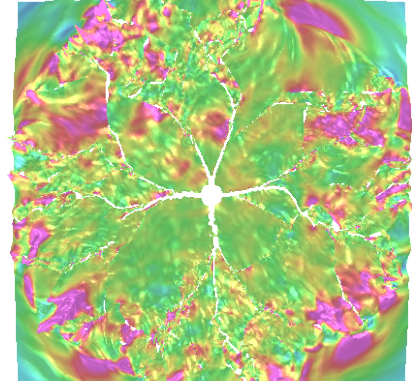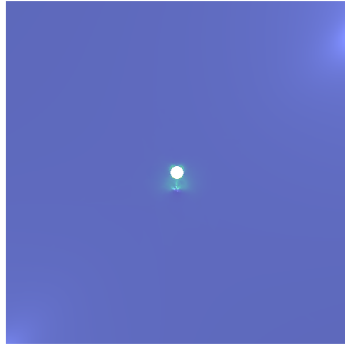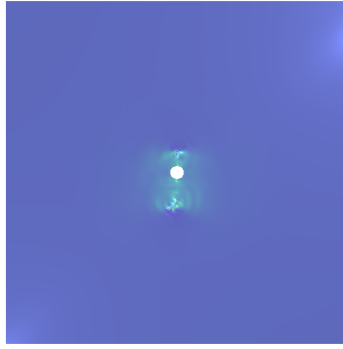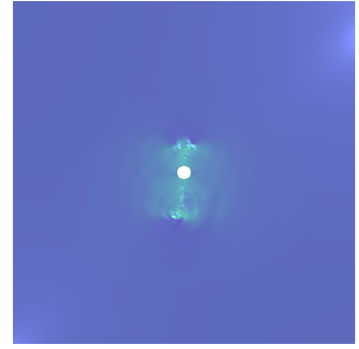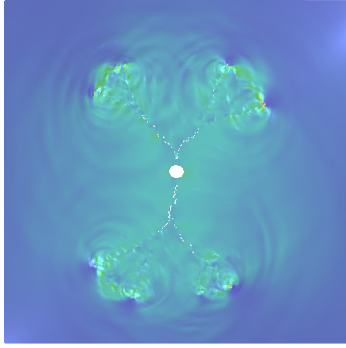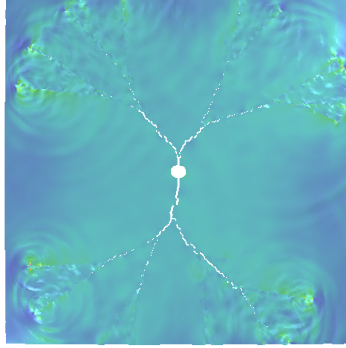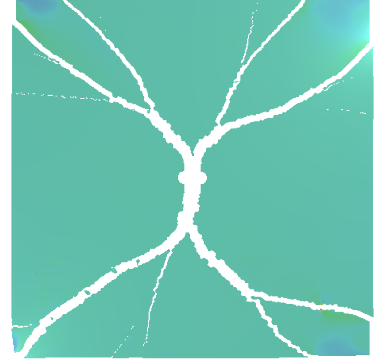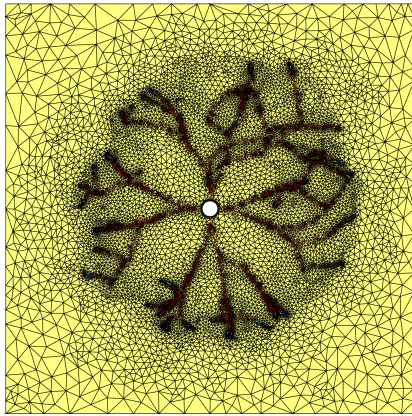
(b) Time $t = 500$ μs.

(c) Time $t = 650$ μs.

(d) Time $t = 800$ μs.

(e) Time $t = 1.2$ ms.

(f) Time $t = 1.7$ ms.

Figure 5: Solution visualization of well stimulation for $t_r = 1$ ms and random nucleation model.

(a) Time $t = 22.00$ ms.

(b) Time $t = 22.25$ ms.

(c) Time $t = 22.35$ ms.
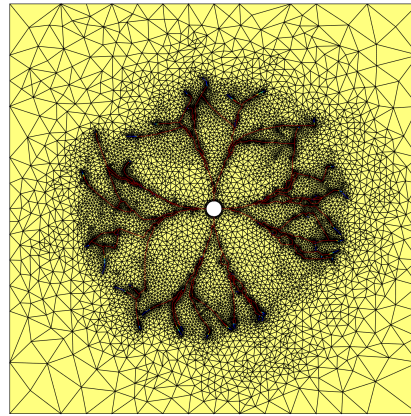
(d) Time $t = 23.25$ ms.

(e) Time $t = 24.00$ ms.

(f) Time $t = 30.00$ ms.

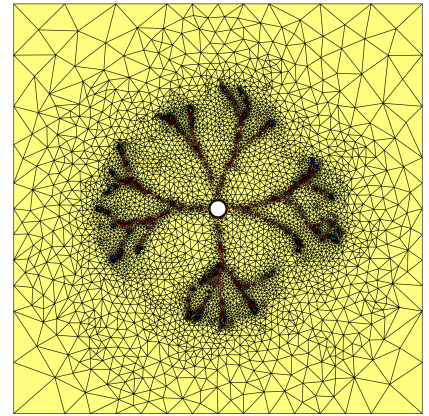Figure 6: Solution visualization of well stimulation for $t_r = 100$ ms and random nucleation model.
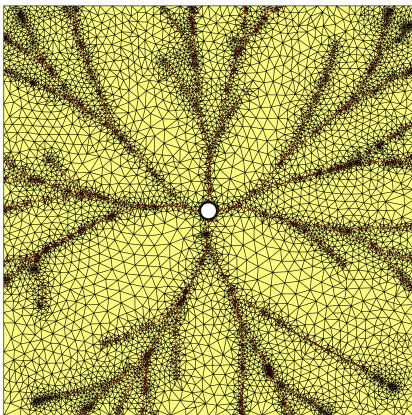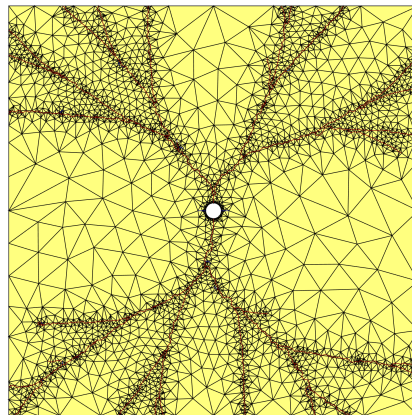

(a) $t_r = 10$ μs / time $t = 800$ μs.
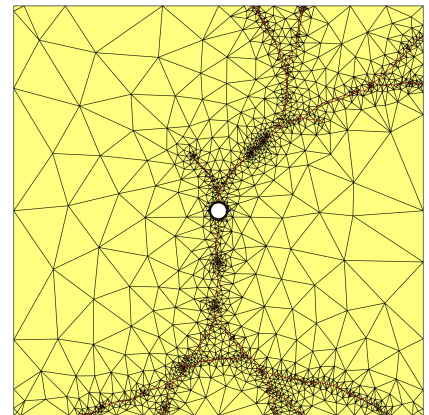
(b) $t_r = 100$ μs / time $t = 800$ μs.

(c) $t_r = 1$ ms / time $t = 1.1$ ms.

(d) $t_r = 10$ ms / time $t = 5.5$ ms.

(e) $t_r = 100$ ms / time $t = 26.5$ ms.

(f) $t_r = 1$ s / time $t = 145$ ms.

Figure 7: Space mesh for different ramp times and random nucleation model with $A_0 = 1$ m^2.
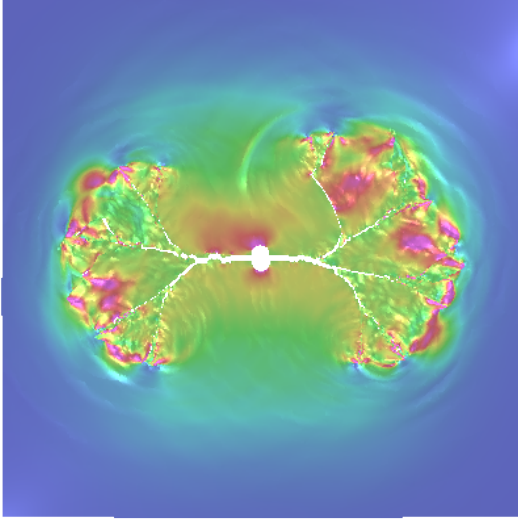
Figure 8: Solution at time $t = 1.1$ ms for ramp time $t_r = 1$ ms and stress anisotropy ratio $r_s = \sigma_H/\sigma_h = \frac{3}{2}$.

We should mention that a reservoir's stress anisotropy can work against crack propagation from all perforations. As an example, we consider the loading with ramp time $t_r = 1$ ms; as shown in fig. 7c for stress anisotropy $r_s = \sigma_H/\sigma_h = 1$, main cracks propagate from all four perforations. Now, if there is a 50% anisotropy, *i.e.*, $r_s = 1.5$, as shown in fig. 8 cracks propagate only from two of the perforations. Although cracks propagate from the two vertical perforations they soon get arrested. Our numerical results, not presented here, demonstrate that the same conclusion can be made for higher loading rates t_r and higher anisotropy ratios r_s. We expect the cases with higher rate of loading to be less sensitive to stress anisotropy, a topic that will be investigated more thoroughly at a later time.

## 3.2 Comparison of deterministic and stochastic nucleation models

The main goal of this section is to demonstrate the importance of using a stochastic model for crack nucleation, particularly under highly transient rates of loading. In fig. 9 we show the results from the deterministic and stochastic nucleation approaches for different ramp times in the left and right columns, respectively. For the fastest loading rate of $t_r = 100$ μs in figs. 9(a-b) we observe that the deterministic approach results in a significantly more complex fracture pattern with substantially more microcracking and crack branching events. We observe the same difference, but to a lesser extent, in figs. 9(c-d); while in this case the overall fracture patterns are similar,

we observe many more microcracking events in fig. 9c. Finally, for the slower loading rates in figs. 9(e-h) we observe that for both approaches cracks propagate only from two of the perforations and there are fewer microcracking and crack branching. This is obviously expected as the loading is becoming less transient. Another observation is that for these slower loading rates, there is less difference between the solutions obtained from the deterministic and stochastic approaches.

The explanation of significant discrepancy between the two approaches at higher loading rates is as follows. When the loads are applied more rapidly, there is less time at the process zones of active cracks or nucleated cracks to accumulate damage. Under this condition large regions experience high stresses. If the material is assumed to have constant fracture strength, cracks will nucleate from many points in these regions. With the stochastic approach the points that have lower strength are nucleated first and the cracks propagates from these points have sufficient time to release stress in neighboring areas that incidentally have higher strength values. This response clearly is closer to what is experienced in real rock, given the distribution of various types of defects that act as nucleation points for crack propagation.

4   CONCLUSIONS

We used the powerful h-adaptive Spacetime Discontinuous Galerkin (SDG) method, along with an interfacial damage model, for modeling dynamic stimulation of rock around a wellbore. We observed that at highly transient modes of loading, cracks propagated from all the four perforations of the wellbore configuration considered. The extent of crack path oscillation, microcracking, and crack bifurcation, *i.e.,* features of dynamic brittle fracture, became less significant as the loading rate decreased. Also, for loading ramp times greater than or equal to 100 ms only two of the four main cracks propagated. Finally, at higher rates of loading the deterministic crack nucleation model, where a constant fracture strength is used, predicted very complex (and less physical) solutions compared with a stochastic approach. This emphasizes the importance of using approaches that do not assume material is macroscopically homogeneous for fracture simulation of brittle materials.
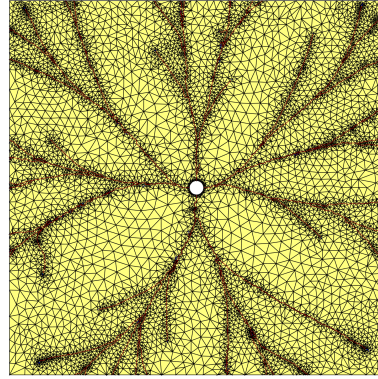
9
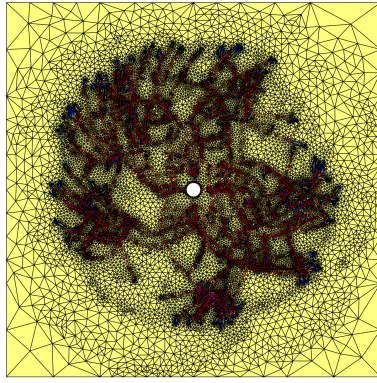
(a) Deterministic nucleation, $t_r = 100$ μs / time $t = 800$ μs.
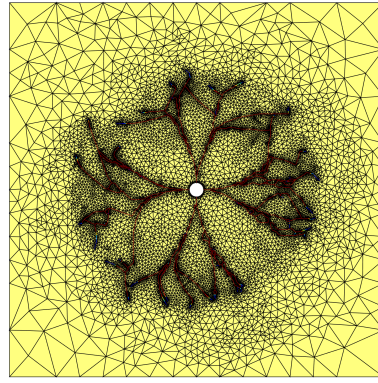
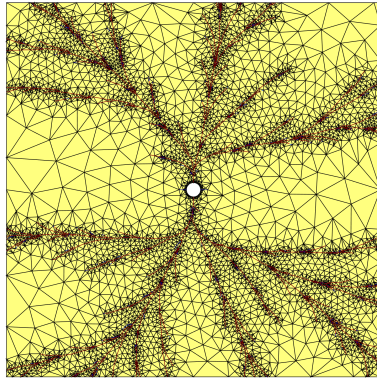(b) Random nucleation, $t_r = 100$ μs / time $t = 800$ μs.
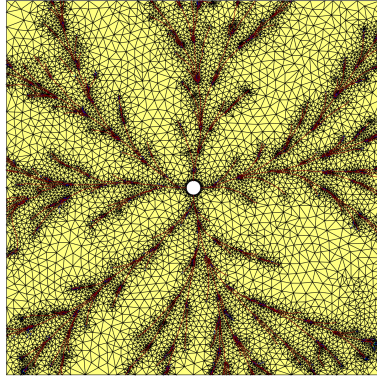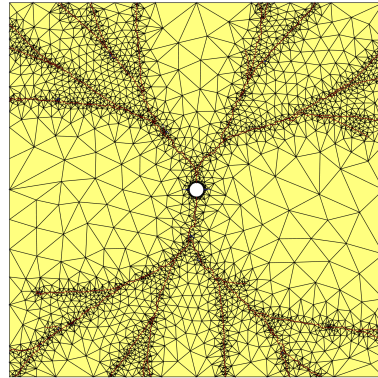
(c) Deterministic nucleation, $t_r = 10$ ms / time $t = 5.5$ ms.

(d) Random nucleation, $t_r = 10$ ms / time $t = 5.5$ ms.

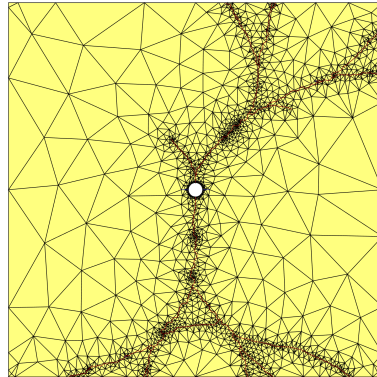(e) Deterministic nucleation, $t_r = 100$ ms / time $t = 26.5$ ms.

(f) Random nucleation, $t_r = 100$ ms / time $t = 26.5$ ms.
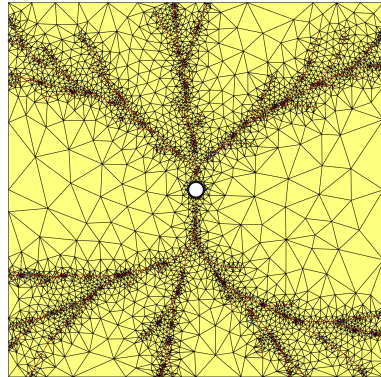
(g) Deterministic nucleation, $t_r = 1$ s / time $t = 140.0$ ms.

(h) Random nucleation, $t_r = 1$ s / time $t = 145.0$ ms.

Figure 9: Comparison of space meshes for deterministic and stochastic nucleation models for different ramp times.

REFERENCES

[1] Dahi-Taleghani, A. and J.E. Olson (2011) Numerical modeling of multistranded-hydraulic-fracture propagation: Accounting for the interaction between induced and natural fractures. *SPE Journal*, **16**, 575–581.

[2] Dahi-Taleghani, A. and J.E. Olson (2014) How natural fractures could affect hydraulic-fracture geometry. *SPE Journal*, **19**, 161–171.

[3] Vishkai, M, G Hareland, ID Gates, et al. (2014) Influence of stress anisotropy on hydraulic fracturing. *48th US Rock Mechanics/Geomechanics Symposium*, American Rock Mechanics Association.

[4] Minaein, Vida, Hassan Bahrami, Md Mofazzal Hossain, Ahmad Jamili, Sadegh Asadi, Reza Rezaee, et al. (2013) Effect of stress anisotropy on well productivity in unconventional gas reservoirs. *SPE Production and Operations Symposium*, Society of Petroleum Engineers.

[5] Tomac, I and M Gutierrez (2015) The effect of loading rate on hydraulic fracturing in synthetic granite-a discrete element study. *AGU Fall Meeting Abstracts*.

[6] Atkinson, C and JM Cook (1993) Effect of loading rate on crack propagation under compressive stress in a saturated porous material. *Journal of Geophysical Research: Solid Earth*, **98**, 6383–6395.

[7] Hanson, JM, RA Schmidt, CH Cooley, JF Schatz, et al. (1984) Multiple fracture stimulation using controlled pulse pressurization. *SPE Unconventional Gas Recovery Symposium*, Society of Petroleum Engineers.

[8] Abedi, R., O. Omidi, and P.L. Clarke (2016) Numerical simulation of rock dynamic fracturing and failure including microscale material randomness. *Proceeding: 50th US Rock Mechanics/Geomechanics Symposium, June 26-June 29, Houston, Texas - USA*, pp. ARMA 16–0531 (13 pages).

[9] Omidi, Omid, Reza Abedi, and Saeid Enayatpour (2016) Well stimulation in tight formations: a dynamic approach. *Proceeding: 50th US Rock Mechanics/Geomechanics Symposium, June 26-June 29, Houston, Texas - USA*, pp. ARMA 16–0150 (12 pages).

[10] Abedi, Reza (2010) *Spacetime damage-based cohesive model for elastodynamic fracture with dynamic contact*. Ph.D. thesis, Department of Theoretical and Applied Mechanics, University of Illinois at Urbana–Champaign.

[11] Omidi, Omid, Reza Abedi, and Saeid Enayatpour (2015) An adaptive meshing approach to capture hydraulic fracturing. *The 49th US Rock Mechanics/Geomechanics Symposium, June 28-July 1, San Francisco,CA,USA*.

[12] Radovitzky, R., A. Seagraves, M. Tupek, and L. Noels (2011) A scalable 3D fracture and fragmentation algorithm based on a hybrid, discontinuous Galerkin, cohesive element method. *Computer Methods in Applied Mechanics and Engineering*, **200**, 326–344.

[13] Abedi, Reza and Robert B. Haber (2014) Riemann solutions and spacetime discontinuous Galerkin method for linear elastodynamic contact. *Computer Methods in Applied Mechanics and Engineering*, **270**, 150 – 177.

[14] Allix, O. and A. Corigliano (1996) Modeling and simulation of crack propagation in mixed modes interlaminar fracture. *International Journal of Fracture*, **77**, 111–140.

[15] Ravi-Chandar, K. and W. G. Knauss (1984) An experimental investigation into dynamic fracture: II: Microstructural aspects. *International Journal of Fracture*, **26**, 65–80.

[16] Ravi-Chandar, K. (1998) Dynamic fracture of nominally brittle materials. *International Journal of Fracture*, **90**, 83–102.

[17] Camacho, G. T. and M. Ortiz (1996) Computational modelling of impact damage in brittle materials. *International Journal of Solids and Structures*, **33**, 2899–2938.

[18] Weibull, W. (1939) A statistical theory of the strength of materials. *R. Swed. Inst. Eng. Res.*, p. Res. 151.

[19] Weibull, W. (1951) A statistical distribution function of wide applicability. *Journal of Applied Mechanics*, **18**, 293–297.

[20] Abedi, Reza, Shuo-Heng Chung, Jeff Erickson, Yong Fan, Michael Garland, Damrong Guoy, Robert Haber, John M. Sullivan, Shripad Thite, and Yuan Zhou (2004) Spacetime meshing with adaptive refinement and coarsening. *Proceedings*

of the Twentieth Annual Symposium on Computational Geometry, June 9-11, pp. 300–309, SCG '04, ACM.

[21] Abedi, Reza, Robert B. Haber, and Boris Petracovici (2006) A spacetime discontinuous Galerkin method for elastodynamics with element-level balance of linear momentum. *Computer Methods in Applied Mechanics and Engineering*, **195**, 3247–3273.

[22] Abedi, R., R. B. Haber, S. Thite, and J. Erickson (2006) An *h*–adaptive spacetime–discontinuous Galerkin method for linearized elastodynamics. *Revue Européenne de Mécanique Numérique (European Journal of Computational Mechanics)*, **15**, 619–642.

[23] Zazovsky, AF et al. (2004) Propellant fracturing revisited. *Gulf Rocks 2004, the 6th North America Rock Mechanics Symposium (NARMS)*, American Rock Mechanics Association.

[24] Zhang, Zhennan, Shujun Peng, Ahmad Ghassemi, Xiurun Ge, et al. (2015) Lattice bond cell modeling of dynamic hydraulic fracture. *49th US Rock Mechanics/Geomechanics Symposium*, American Rock Mechanics Association.

[25] Mohammadnejad, T. and J.E. Andrade (2016) Numerical modeling of hydraulic fracture propagation, closure and reopening using XFEM with application to in-situ stress estimation. *International Journal for Numerical and Analytical Methods in Geomechanics*, **40**, 2033–2060.